Published in IET Signal Processing
Received on 1st August 2012
Revised on 9th May 2013
Accepted on 29th May 2013
doi: 10.1049/iet-spr.2012.0227

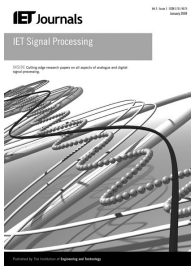

ISSN 1751-9675

Signal recognition and adapted filtering by non-commutative tomography

Carlos Aguirre[1], *Rui Vilela Mendes*[2,3]

[1]*GNB, Escuela Politécnica Superior, Universidad Autonoma de Madrid, Campus de Cantoblanco, Ctra de Colmenar Km 16, 28049 Madrid, Spain*
[2]*CMAF, Complexo Interdisciplinar, Av. Gama Pinto 2, 1649-003 Lisboa, Portugal*
[3]*IPFN, Instituto Superior Técnico, Av. Rovisco Pais 1, 1049-001 Lisboa, Portugal*
E-mail: rvilela.mendes@gmail.com

Abstract: Tomogram, a generalisation of the Radon transform to arbitrary pairs of non-commuting operators, is a positive bilinear transforms with a rigorous probabilistic interpretation which provides a full characterisation of the signal and is robust in the presence of noise. Tomograms based on the time–frequency operator pair, were used in the past for component separation and denoising. Here the authors show that, even for noisy signals, meaningful time-resolved information may be obtained by the construction of an operator pair adapted to the signal.

1 Introduction

1.1 Integral transforms: linear, bilinear and tomograms

Data analysis establishes the fundamental link between active measurements or received signals and the conclusions and messages that can be extracted from them. Signal processing in communications, engineering, medicine and physics relies heavily on integral transforms [1, 2]. Linear transforms, such as Fourier [3] and wavelets [4–6] are the most popular. These are most appropriate for stationary signals with stable frequency or size scale structures. However, because many signals in nature are highly non-stationary other tools were developed, in particular bilinear transforms such as the Wigner–Ville (WV) quasi-distribution [7, 8] and the short-time Fourier transform (STFT). STFT is useful to characterise non-stationary signals as long as they are piece-wise stationary. Both WV and STFT provide information in the joint time–frequency domain, which is indeed relevant because in many applications (biomedical, seismic, radar etc.) the signals are of finite (sometimes very short) duration. However, the negative amplitudes and oscillating cross-terms in the WV and other quasi-distributions [9–11] make the interpretation of the transformed signals a difficult matter. Even when the average of the cross-terms is small, their amplitude may be greater than the signal in time–frequency regions that carry no physical information.

The difficulties with the physical interpretation of quasi-distributions arise from the fact that time and frequency correspond to two non-commutative operators. Hence, a joint probability density can never be defined. Even in the case of positive quasi-probabilities such as the Husimi–Kano function [12, 13], an interpretation as a joint probability distribution is also not possible because the two arguments in the function are not simultaneously measurable random variables.

Recently, a new type of strictly positive bilinear transform has been proposed [14–16], called a tomogram, which is a generalisation of the Radon transform [17] to arbitrary non-commutative pairs of operators. The Radon–Wigner transform [18, 19] is a particular case of the non-commutative tomography technique. Being strictly positive probability densities, the tomograms provide a full characterisation of the signal and are robust in the presence of noise.

A unified framework to characterise linear transforms, quasi-distributions and tomograms was developed in [15]. To fix notation we briefly review it here. Signals $\boldsymbol{f(t)}$ are considered as vectors $|f\rangle$ in a subspace $\mathcal{N}$ of a Hilbert space $\mathcal{H}$ with dual space $\mathcal{N}^*$. Then a family of unitary operators $U(\alpha) = e^{iB(\alpha)}$, α being a label $\{\alpha \in I, I \subset \mathbb{R}^n\}$, is defined on $\mathcal{N}^*$. Using a ket-bra notation we denote $|f\rangle \in \mathcal{N}$ and $\langle f| \in \mathcal{N}^*$. In this setting three types of integral transforms are constructed. Let $h \in \mathcal{N}^*$ be a reference vector and let U be such that the linear span of $\{U(\alpha)h \in \mathcal{N}^* : \alpha \in I\}$ is dense in $\mathcal{N}^*$. In $\{U(\alpha)h\}$, a complete set of vectors can be chosen to serve as basis.

1. Linear transforms

$$W_f^{(h)}(\alpha) = \langle U(\alpha)h|f\rangle \tag{1}$$

2. Quasi-distributions

$$Q_f(\alpha) = \langle U(\alpha)f|f\rangle \tag{2}$$

3. Tomograms: Given a unitary $U(\alpha) = e^{iB(\alpha)}$, $B(\alpha)$ has the spectral decomposition $B(\alpha) = \int XP(X)dX$. Let

$$P(X) \stackrel{\circ}{=} |X\rangle\langle X|$$

denote the projector on the (generalised) eigenvector $\langle X| \in \mathcal{N}^*$ of $B(\alpha)$. The tomogram is

$$M_f^{(B)}(X) = \langle f|P(X)|f\rangle = \langle f|X\rangle\langle X|f\rangle = |\langle X|f\rangle|^2 \quad (3)$$

[Another convenient notation for the projector on a generalised eigenvector of $B(\alpha)$ with eigenvalue X is $\delta(B(\alpha) - X) \stackrel{\circ}{=} P(X)$]

The tomogram $M_f^{(B)}(X)$ is the squared amplitude of the projection of the signal $|f\rangle \in \mathcal{N}$ on the eigenvector $\langle X| \in \mathcal{N}^*$ of the operator $B(\alpha)$. Therefore it is positive. For normalised $|f\rangle$

$$\langle f|f\rangle = 1$$

the tomogram is normalised

$$\int M_f^{(B)}(X)\mathrm{d}X = 1 \quad (4)$$

and may be interpreted as a probability distribution on the set of generalised eigenvalues of $B(\alpha)$, that is, as the probability distribution for the random variable X corresponding to the observable defined by the operator $B(\alpha)$.

The tomogram is a homogeneous function

$$M_f^{(B/p)}(X) = |p|M_f^{(B)}(pX) \quad (5)$$

Examples: If $U(\alpha)$ is unitary, generated by $B_F(\boldsymbol{\alpha}) = \alpha_1 t + i\alpha_2(d/\mathrm{d}t)$ and h is a (generalised) eigenvector of the time-translation operator the linear transform $W_f^{(h)}(\alpha)$ is the Fourier transform. For the same $B_F(\boldsymbol{\alpha})$, the quasi-distribution $Q_f(\alpha)$ is the ambiguity function and the WV transform [7, 8] is the quasi-distribution $Q_f(\alpha)$ for the following B-operator

$$B^{(\mathrm{WV})}(\alpha_1, \alpha_2) = -i2\alpha_1 \frac{d}{\mathrm{d}t} - 2\alpha_2 t + \frac{\pi\left(t^2 - \left(\left(d^2\right)/\left(\mathrm{d}t^2\right)\right) - 1\right)}{2} \quad (6)$$

The wavelet transform is $W_f^{(h)}(\alpha)$ for $B_W(\boldsymbol{\alpha}) = \alpha_1 D + i\alpha_2(d/\mathrm{d}t)$, D being the dilation operator $D = -1/2(it(d/\mathrm{d}t) + i(d/\mathrm{d}t)t)$. The wavelets $h_{s,\tau}(t)$ are kernel functions generated from a basic wavelet $h(\tau)$ by means of a translation and a rescaling $(-\infty < \tau < \infty,\ s > 0)$

$$h_{s,\tau}(t) = \frac{1}{\sqrt{s}} h\left(\frac{t-\tau}{s}\right) \quad (7)$$

using the operator

$$U^{(A)}(\tau, s) = \exp(i\tau\hat{\omega}) \exp(i \log sD) \quad (8)$$

$$h_{s,\tau}(t) = U^{(A)\dagger}(\tau, s)h(t) \quad (9)$$

The Bertrand transform [20, 21] is the quasi-distribution $Q_f(\alpha)$ for B_W. Linear, bilinear and tomogram transforms are related to one another (see [15]).

As a final remark to this introduction, note that the transforms discussed so far rely on the assumption that frequency or scale structures are the relevant features to extract from the signals. This means that the structures to be sifted out from the signal are chosen apriori, frequencies or size scales corresponding to the particular wavelets being used. Also the Huang–Hilbert transform [22], that is being increasingly used, may be thought of as a generalised Fourier decomposition, because it describes a signal in terms of basis functions whose amplitudes and frequencies may fluctuate with time.

The main purpose of this paper is to develop a signal-adapted tomogram as a flexible tool where the features to be extracted from the signal may be adjusted at will. After describing briefly how the tomograms are built and used in Sections 2 and 3 the signal-adapted tomogram is constructed in Section 4.

1.2 Tomograms: some examples

As shown before, tomograms are obtained from projections on the eigenstates of the B operators. These operators may be linear combinations of different (commuting or non-commuting) operators

$$B = \mu O_1 + \nu O_2$$

meaning that the tomogram explores the signal along lines in the plane (O_1, O_2). For example, for

$$B(\mu, \nu) = \mu t + \nu\omega = \mu t + i\nu\frac{\mathrm{d}}{\mathrm{d}t}$$

the tomogram is the expectation value of a projection operator with support on a line in the time–frequency plane

$$X = \mu t + \nu\omega \quad (10)$$

Therefore $M_f^{(S)}(X, \mu, \nu)$ is the marginal distribution of the variable X along this line in the time–frequency plane. The line is rotated and rescaled when one changes the parameters μ and ν. In this way, the whole time–frequency plane is sampled and the tomographic transform contains all the information on the signal. Instead of marginals collected along straight lines on the time–frequency plane, one may use other curves to sample this space [15].

Tomograms associated to the generators of the conformal group:

Time–frequency

$$B_1 = \mu t + i\nu\frac{\mathrm{d}}{\mathrm{d}t} \quad (11)$$

doi: 10.1049/iet-spr.2012.0227

Time-scale

$$B_2 = \mu t + i\nu\left(t\frac{\mathrm{d}}{\mathrm{d}t} + \frac{1}{2}\right) \tag{12}$$

Frequency-scale

$$B_3 = i\mu\frac{\mathrm{d}}{\mathrm{d}t} + i\nu\left(t\frac{\mathrm{d}}{\mathrm{d}t} + \frac{1}{2}\right) \tag{13}$$

Time-conformal

$$B_4 = \mu t + i\nu\left(t^2\frac{\mathrm{d}}{\mathrm{d}t} + t\right) \tag{14}$$

The construction of the tomograms reduces to the calculation of the generalised eigenvectors of each one of the B_i operators

$$\begin{aligned} B_1\psi_1(\mu, \nu, t, X) &= X\psi_1(\mu, \nu, t, X) \\ \psi_1(\mu, \nu, t, X) &= \exp i\left(\frac{\mu t^2}{2\nu} - \frac{tX}{\nu}\right) \end{aligned} \tag{15}$$

with normalisation

$$\int \mathrm{d}t\psi_1^*(\mu, \nu, t, X)\psi_1(\mu, \nu, t, X') = 2\pi\nu\delta(X - X') \tag{16}$$

$$\begin{aligned} B_2\psi_2(\mu, \nu, t, X) &= X\psi_2(\mu, \nu, t, X) \\ \psi_2(\mu, \nu, t, X) &= \frac{1}{\sqrt{|t|}}\exp i\left(\frac{\mu t}{\nu} - \frac{X}{\nu}\log|t|\right) \end{aligned} \tag{17}$$

$$\int \mathrm{d}t\psi_2^*(\mu, \nu, t, X)\psi_2(\mu, \nu, t, X') = 4\pi\nu\delta(X - X') \tag{18}$$

$$\begin{aligned} B_3\psi_3(\mu, \nu, \omega, X) &= X\psi_3(\mu, \nu, \omega, X) \\ \psi_3(\mu, \nu, t, X) &= \exp(-i)\left(\frac{\mu}{\nu}\omega - \frac{X}{\nu}\log|\omega|\right) \end{aligned} \tag{19}$$

$$\int d\omega\psi_1^*(\mu, \nu, \omega, X)\psi_1(\mu, \nu, \omega, X') = 2\pi\nu\delta(X - X') \tag{20}$$

$$\begin{aligned} B_4\psi_4(\mu, \nu, t, X) &= X\psi_4(\mu, \nu, t, X) \\ \psi_4(\mu, \nu, t, X) &= \frac{1}{|t|}\exp i\left(\frac{X}{\nu t} + \frac{\mu}{\nu}\log|t|\right) \end{aligned} \tag{21}$$

$$\int \mathrm{d}t\psi_4^*(\mu, \nu, t, s)\psi_4(\mu, \nu, t, s') = 2\pi\nu\delta(s - s') \tag{22}$$

Then the tomograms are:

Time–frequency tomogram

$$M_1(\mu, \nu, X) = \frac{1}{2\pi|\nu|}\left|\int \exp\left[\frac{i\mu t^2}{2\nu} - \frac{itX}{\nu}\right]f(t)\mathrm{d}t\right|^2 \tag{23}$$

Time-scale tomogram

$$M_2(\mu, \nu, X) = \frac{1}{2\pi|\nu|}\left|\int \mathrm{d}t\frac{f(t)}{\sqrt{|t|}}\mathrm{e}^{\left[i\left((\mu/\nu)t - (X/\nu)\log|t|\right)\right]}\right|^2 \tag{24}$$

Frequency-scale tomogram

$$M_3(\mu, \nu, X) = \frac{1}{2\pi|\nu|}\left|\int \mathrm{d}\omega\frac{f(\omega)}{\sqrt{|\omega|}}\mathrm{e}^{\left[-i\left((\mu/\nu)\omega - (X/\nu)\log|\omega|\right)\right]}\right|^2 \tag{25}$$

$f(\omega)$ being the Fourier transform of $f(t)$

Time-conformal tomogram

$$M_4(\mu, \nu, X) = \frac{1}{2\pi|\nu|}\left|\int \mathrm{d}t\frac{f(t)}{|t|}\mathrm{e}^{\left[i\left((X/\nu t) + (\mu/\nu)\log|t|\right)\right]}\right|^2 \tag{26}$$

The tomograms M_1, M_2 and M_4 interpolate between the (squared) time signal ($\nu = 0$) and its projection on the $\psi_i(\mu, \nu, t, X)$ functions for $\mu = 0$.

In a similar way, tomograms may be constructed for any operator of the general type

$$B_4 = \mu t + i\nu\left(g(t)\frac{\mathrm{d}}{\mathrm{d}t} + \frac{1}{2}\frac{\mathrm{d}g(t)}{\mathrm{d}t}\right)$$

the generalised eigenvectors being

$$\psi_g(\mu, \nu, t, X) = |g(t)|^{-1/2}\exp i\left(-\frac{X}{\nu}\int\frac{\mathrm{d}s}{g(s)} + \frac{\mu}{\nu}\int\frac{s\mathrm{d}s}{g(s)}\right)$$

When dealing with finite-time signals and finite-time tomograms some normalisation modifications are needed. For example, for a time–frequency tomogram, instead of (23), we consider the finite-time tomogram, for a signal defined from t_0 to $t_0 + T$

$$M_1(\theta, X) = \left|\int_{t_0}^{t_0+\mathrm{T}} f^*(t)\psi_{\theta,X}^{(1)}(t)\mathrm{d}t\right|^2 = \left|\langle f, \psi^{(1)}\rangle\right|^2 \tag{27}$$

with

$$\psi_{\theta,X}^{(1)}(t) = \frac{1}{\sqrt{T}}\exp\left(\frac{i\cos\theta}{2\sin\theta}t^2 - \frac{iX}{\sin\theta}t\right) \tag{28}$$

and $\mu = \cos\theta$, $\nu = \sin\theta$. θ is a parameter that interpolates between the time and the frequency operators, running from 0 to $\pi/2$, whereas X is allowed to be any real number. An orthonormalised set of $\psi_{\theta,X}^{(1)}(t)$ vectors is obtained by choosing the sequence

$$X_n = X_0 + \frac{2n\pi}{T}\sin\theta, \quad n \in \mathbb{Z} \tag{29}$$

Likewise for the finite-time time-scale tomogram $M_2(\mu, \nu, X)$ (24) and the finite-time time-conformal tomogram $M_4(\mu,$

ν, X) (26)

$$M_2(\theta, X) = \left| \int_{t_0}^{t_0+\mathrm{T}} f^*(t)\psi^{(2)}_{\theta,X}(t)\mathrm{d}t \right|^2 = \left|\langle f, \psi^{(2)}\rangle\right|^2 \quad (30)$$

$$\psi^{(2)}_{\theta,X}(t) = \frac{1}{\sqrt{\log|t_0+T| - \log|t_0|}} \frac{1}{\sqrt{|t|}} \times \exp i\left(\frac{\cos\theta}{\sin\theta}t - \frac{X}{\sin\theta}\log|t|\right) \quad (31)$$

$$X_n = X_0 + \frac{2n\pi}{\log|t_0+T| - \log|t_0|}\sin\theta, \quad n \in \mathbb{Z} \quad (32)$$

and

$$M_4(\theta, X) = \left| \int_{t_0}^{t_0+T} f^*(t)\psi^{(4)}_{\theta,X}(t)\mathrm{d}t \right|^2 = \left|\langle f, \psi^{(4)}\rangle\right|^2 \quad (33)$$

$$\psi^{(4)}_{\theta,X}(t) = \sqrt{\frac{t_0(t_0+T)}{T}} \frac{1}{|t|} \exp i\left(\frac{\cos\theta}{\sin\theta}\log|t| + \frac{X}{t\sin\theta}\right) \quad (34)$$

$$X_n = X_0 + \frac{t_0(t_0+T)}{T} 2\pi n \sin\theta, \quad n \in \mathbb{Z} \quad (35)$$

Tomograms performing a signal analysis on two variables (time and frequency, time and scale etc.) are more powerful than linear transforms such as Fourier or wavelets. On the other hand, in contrast with the bilinear transforms (WV, Bertrand etc.) and because of their rigorous probabilistic interpretation, they provide a robust and unambiguous characterisation of the signals.

2 Applications of tomograms: denoising and component separation

Most natural and man-made signals are non-stationary and have a multicomponent structure. Therefore separation of its components is an issue of great technological relevance. However, the concept of signal component is not uniquely defined. The notion of component depends as much on the observer as on the observed object. When we speak about a component of a signal we are in fact referring to a particular feature of the signal that we want to emphasise. For signals that have distinct features both in time and in the frequency domain, the time-frequency tomogram is an appropriate tool.

Consider finite-time tomograms as in (27). For all different θs the $U(\theta)$, of which $B(\theta)$ is the self-adjoint generator, are unitarily equivalent operators, hence all the tomograms share the same information.

To perform the tomographic projection (3) it is important to project into an orthonormal set. Therefore the first step is to select a subset X_n in such a way that the corresponding family $\left\{\psi^{(1)}_{\theta,X_n}(t)\right\}$ is orthogonal and normalised

$$\langle \psi^{(1)}_{\theta,X_n} \psi^{(1)}_{\theta,X_m}\rangle = \delta_{m,n} \quad (36)$$

It follows from (28) that

$$\langle \psi^{(1)}_{\theta,X_n} \psi^{(1)}_{\theta,X_m}\rangle = \frac{\sin\theta}{iT(X_n - X_m)} \times \left\{\exp\left(\frac{iT}{\sin\theta}(X_n - X_m)\right) - 1\right\}$$

and using (36) one concludes that the required sequence X_n is the one listed in (29), where X_0 is freely chosen (in general we take $X_0 = 0$). We then consider the projections of the signal $f(t)$ on this set of $\psi^{(1)}_{\theta,X_n}$ vectors

$$c^{\theta}_{X_n}(f) = \langle f, \psi^{(1)}_{\theta,X_n}\rangle \quad (37)$$

Denoising consists in eliminating the $c^{\theta}_{X_n}(f)$ such that

$$\left|c^{\theta}_{X_n}(f)\right|^2 \le \varepsilon \quad (38)$$

for some threshold ε. This power selective denoising is more robust than, for example, frequency filtering which may also eliminate important signal information.

The component separation technique is based on the search for an intermediate value of θ where a good compromise might be found between time localisation and frequency information. This is achieved by selecting subsets $\mathcal{F}_k$ of the X_n and reconstructing partial signals (k-components) by restricting the sum to

$$f_k(t) = \sum_{n\in\mathcal{F}_k} c^{\theta}_{X_n}(f)\psi_{\theta,X_n}(t) \quad (39)$$

for each k. For examples on how the $\mathcal{F}_k$ subsets are chosen we refer to [23]. Note that, in all cases, component separation has been done by direct visual inspection of the contour plot of the full tomogram. An automatic procedure to perform this separation, by examining intensity peaks is, in principle, possible but has not yet been implemented.

3 Signal detection with an adapted operator pair

Time–frequency tomograms have been used for denoising and component separation of finite-time signals [14, 23–26]. Time–frequency tomograms are particularly appropriate to identify the time unfolding of the frequency features of the signals. For example, the component separation success [23, 24] in the plasma reflectometry applications is to a large extent due to the fact that the plasma is sampled by microwave chirps and the basis in (28) is exactly a chirp basis. This suggests that, for other types of signals, other types of tomograms should be chosen.

In particular, in the linear combination $B(\mu, \nu) = \mu t + \nu O$, one might choose an operator O tuned to the signal features that one wants to extract. Then, by looking for particular values in the set (μ, ν) where noise effects cancel out, we may not only separate the information of small signals from noise but also obtain reliable information on the temporal structure of the signal. This would be a signal-adapted filtering technique. The construction of an operator suited to particular signals may be done by the same techniques that are used in the bi-orthogonal decomposition [27].

doi: 10.1049/iet-spr.2012.0227

The method for the construction of the adapted operator pair is as follows:

Consider a set of N-dimensional time sequences $\{\boldsymbol{x}_1, \ldots, \boldsymbol{x}_k\}$, typical of the signal features one wants to detect. From a communication point of view these may be considered as the code words that one wishes to detect in the noisy signal. Form the $k \times N$ matrix $U \in \mathcal{M}_{k\times N}$

$$U = \begin{pmatrix} x_1(1\Delta t) & x_1(2\Delta t) & \ldots & x_1(N\Delta t) \\ \vdots & \vdots & & \vdots \\ x_k(1\Delta t) & x_k(2\Delta t) & \ldots & x_k(N\Delta t) \end{pmatrix} \tag{40}$$

with typically $k < N$.

Now construct the square matrices $A = U^T U \in \mathcal{M}_{N\times N}$ and $B = UU^T \in \mathcal{M}_{k\times k}$. The diagonalisation of A provides k non-zero eigenvalues $(\alpha_1, \ldots, \alpha_k)$ and its corresponding orthogonal N-dimensional eigenvectors $(\Phi_1, \ldots, \Phi_k)$, $\Phi_j \in \mathbb{R}^N$. The diagonalisation of B would provide the same k eigenvalues and eigenvectors $(\Psi_1, \ldots, \Psi_k)$ with $\Psi_j \in \mathbb{R}^k$. If needed one may obtain, by the Gram–Schmidt method, the remaining N–k eigenvectors to span $\mathbb{R}^N$, which in this context are associated to the eigenvalue zero.

The linear operator S constructed from the set of typical signals is

$$S = \sum_{i=1}^{k} \alpha_i \Phi_i \Phi_i^t \tag{41}$$

where $S \in \mathcal{M}_{N\times N}$.

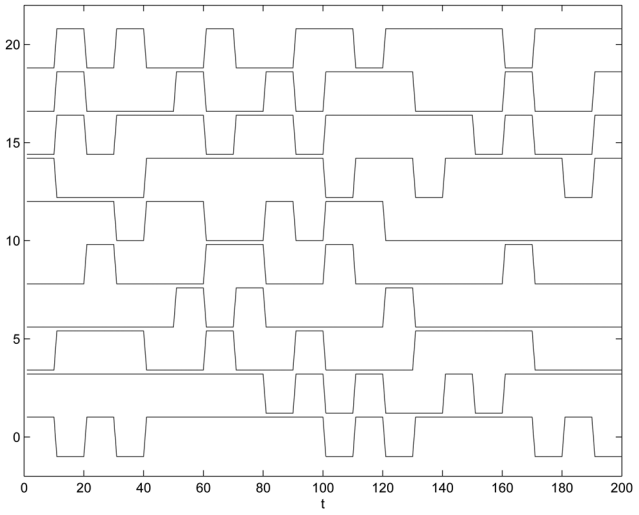

Fig. 1 *Set of typical signals*

For the tomogram we consider an operator $B(\mu, \nu)$ of the form

$$B(\mu, \nu) = \mu t + \nu S = \mu \begin{pmatrix} 1\Delta t & & & & \\ & 2\Delta t & & & \\ & & 3\Delta t & & \\ & & & \ddots & \\ & & & & N\Delta t \end{pmatrix} + \nu \sum_{i=1}^{k} \alpha_i \Phi_i \Phi_i^t \tag{42}$$

where $B \in \mathcal{M}_{N\times N}$.

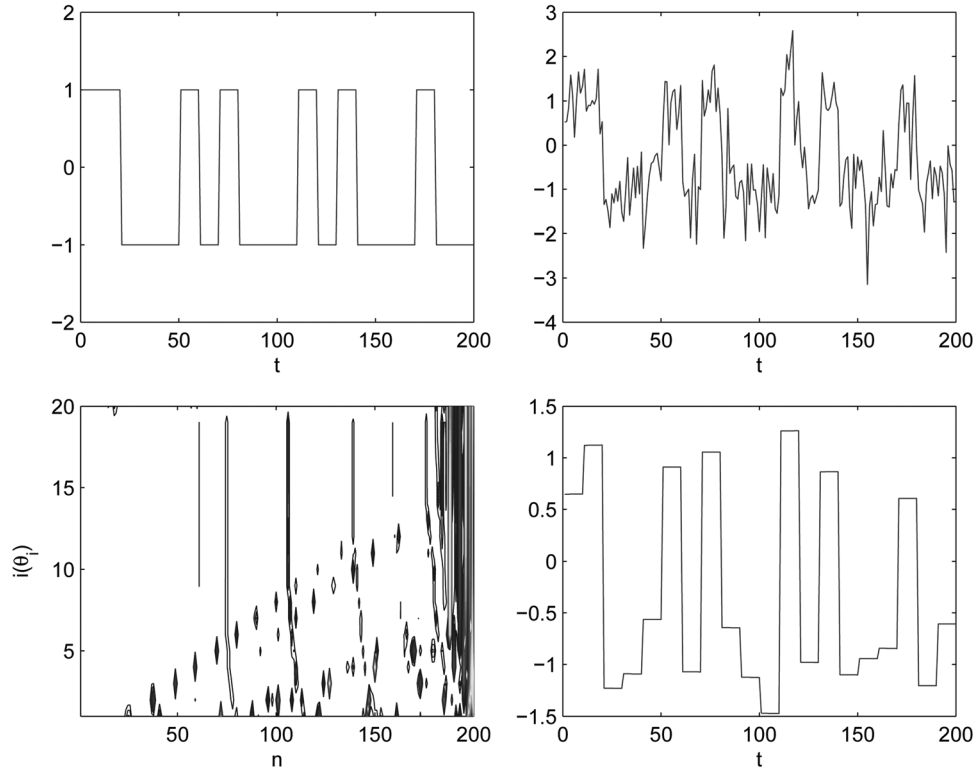

Fig. 2 *Signal, noisy signal, the tomogram and the projection on the subspace spanned by the eigenvectors 185–200 at $\theta = 19\pi/40$*

The eigenvectors of each $B(\mu, \nu)$ are the columns of the matrix that diagonalises it. Taking the projections of the signal on these eigenvectors one obtains a tomogram adapted to the operator pair (t, S).

3.1 Examples

Here, we present some examples of the application of the technique described in the previous section.

In the first example a set of 40 random signals with pulses of duration $\Delta t = 10$ and intensities $+1$ or -1 are generated. The total length of the signal is 200 time units. These random signals form the typical data to which we will adapt the tomogram, by constructing the operator S in (41). Fig. 1 shows 10 signals of this type. They all vary between $+1$ and -1, being shifted in the figure for clarity purposes.

Once the operator S is constructed, one considers the operator

$$B(\theta) = t\cos\theta + S\sin\theta$$

for which one computes the eigenbasis which is used to project the signals to be analysed. To a pure signal of the same type as those used to construct the operator S (in the upper left panel of Fig. 2), we have added Gaussian noise (upper right panel of Fig. 2). This signal is then analysed and a tomogram constructed for 20 different values of θ at intervals $\Delta\theta = \pi/40$. A contour plot of the tomogram is shown in the lower left panel of Fig. 2. As we have explained before, by inspection of the power distribution in the tomogram one may either select the components of intensity higher than a threshold for denoising of the whole signal or select particular components of signal. In this case, what is of interest is to select the part of the signal that corresponds to the typical signals used to construct S. This is done by selecting only the strongest components at the region where they concentrate. In the lower right panel of Fig. 2, we show the result of projecting on the subspace spanned by the eigenvectors 185–200 at $\theta_{19} = 19\pi/40$.

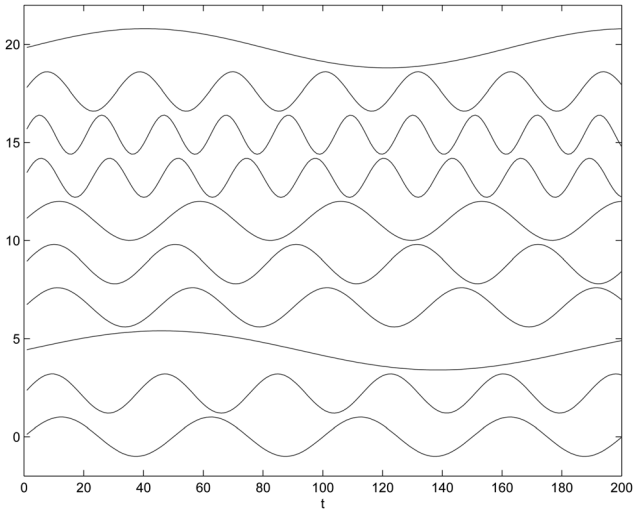

Fig. 3 *Set of sines with random frequencies*

One sees that the signal is reasonably reconstructed from the noisy input. With a clipping operation at ± 0.5 the reconstruction would be perfect.

For the second example, we have generated, as typical signals a set of 40 sines with random frequencies. Fig. 3 displays some examples.

This case is harder because noise (or interference) is expected to contain frequencies similar to the typical signals. Fig. 4 shows the results of the analysis of a signal that contains pieces of sines at different time intervals. The signal is displayed in the upper left panel and the signal with added Gaussian noise in the upper right panel. The

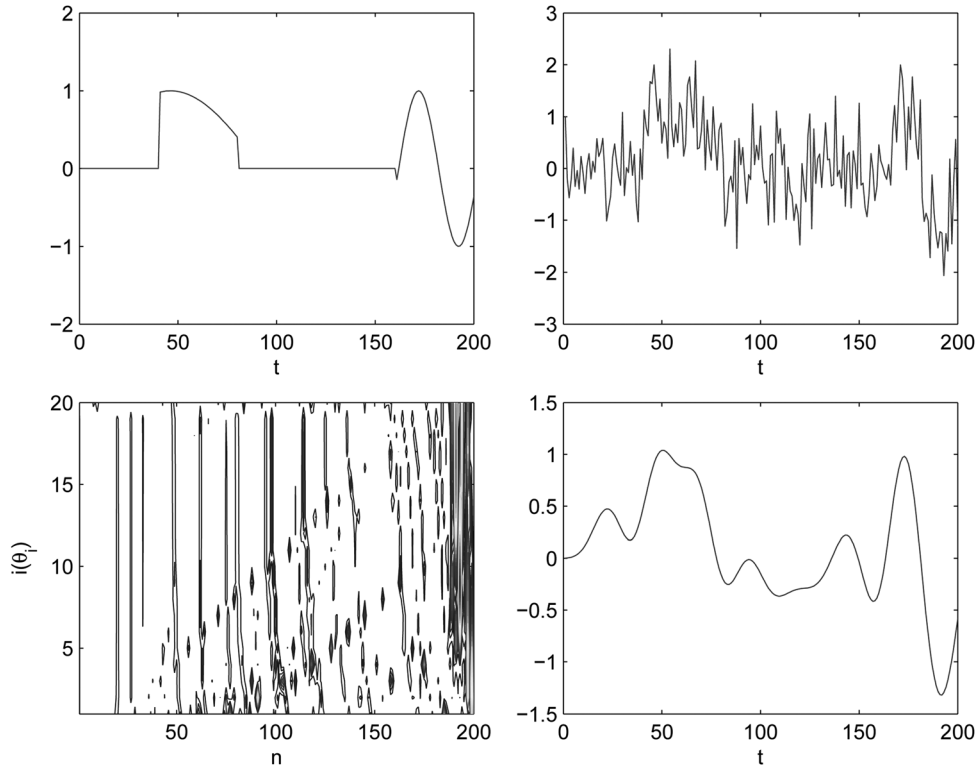

Fig. 4 *Signal, noisy signal, the tomogram and the projection on the subspace spanned by the eigenvectors 189–197 at $\theta = 19\pi/40$*

doi: 10.1049/iet-spr.2012.0227

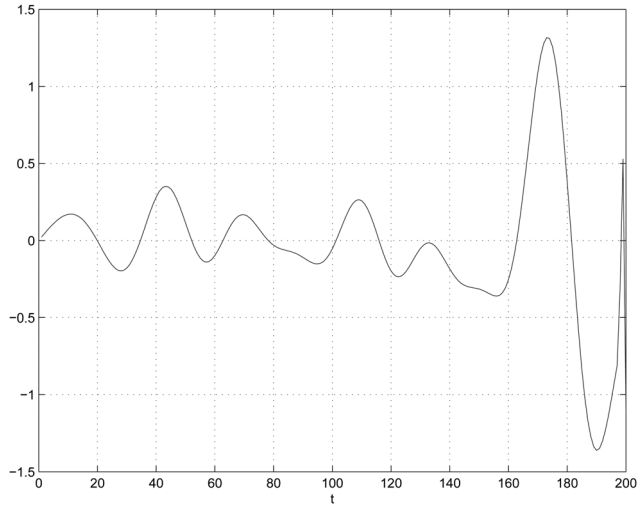

Fig. 5 *Projection on the subspace spanned by the eigenvectors 190–199 at $\theta = \pi/10$ which separates the second time component of the signal*

tomogram is in the lower left panel and in the lower right panel the result of the projection on the subspace spanned by the eigenvectors 189–197 at $\theta_4 = 15\pi/40$.

The projection range that was used includes all the strongest components. Note, however, that by selecting particular regions of the tomogram, particular components of the signal may be extracted. For example, Fig. 5 shows the result of projection on the subspace spanned by the eigenvectors 190–199 at $\theta = \pi/10$.

For the third example, we use data obtained from the Phoenix Mars Lander [28]. A dust devil is a hot whirlwind generated by a huge temperature contrast between the martian atmospheric air and the planet surface. Dust devils appear in both temperature and pressure data as sudden drops with a duration between 2 and 3 min. The upper left panel in Fig. 6 shows some data from the Phoenix Mars Lander covering a 2000 s interval with a sampling rate of 0.5 Hz. A dust devil is clearly visible at $t \simeq 800$ s as a drop in the pressure value.

There has been several efforts to develop systematic methods to detect the effect of dust devils on the martian atmosphere data. They are based either on checking several *ad-hoc* conditions in the data [28] or on field-programmable gate arrays [29].

To use our adapted tomographic filtering method for the detection of dust devils we have generated a set of 278 signals that resemble the shape that a dust devil produces on the data, that is a sudden drop of about 3% from the baseline, with different durations ranging from 60 to 80 time units. The upper right panel displays several of these typical signals. Some of the signals have been shifted up or down for representation purposes.

As in the previous examples a tomogram is constructed for 20 different values of θ at intervals $\Delta\theta = \pi/40$. A contour plot of the first 999 coefficients of the tomogram is shown in the lower left panel of Fig. 6. Coefficient $n = 1000$ corresponds to the biggest eigenvalue (and its corresponding eigenvector). This eigenvector contains most of the energy of the signal, and is several orders of magnitude bigger that any other coefficient, so for clarity this coefficient has not been plotted in the tomogram. By direct inspection, we

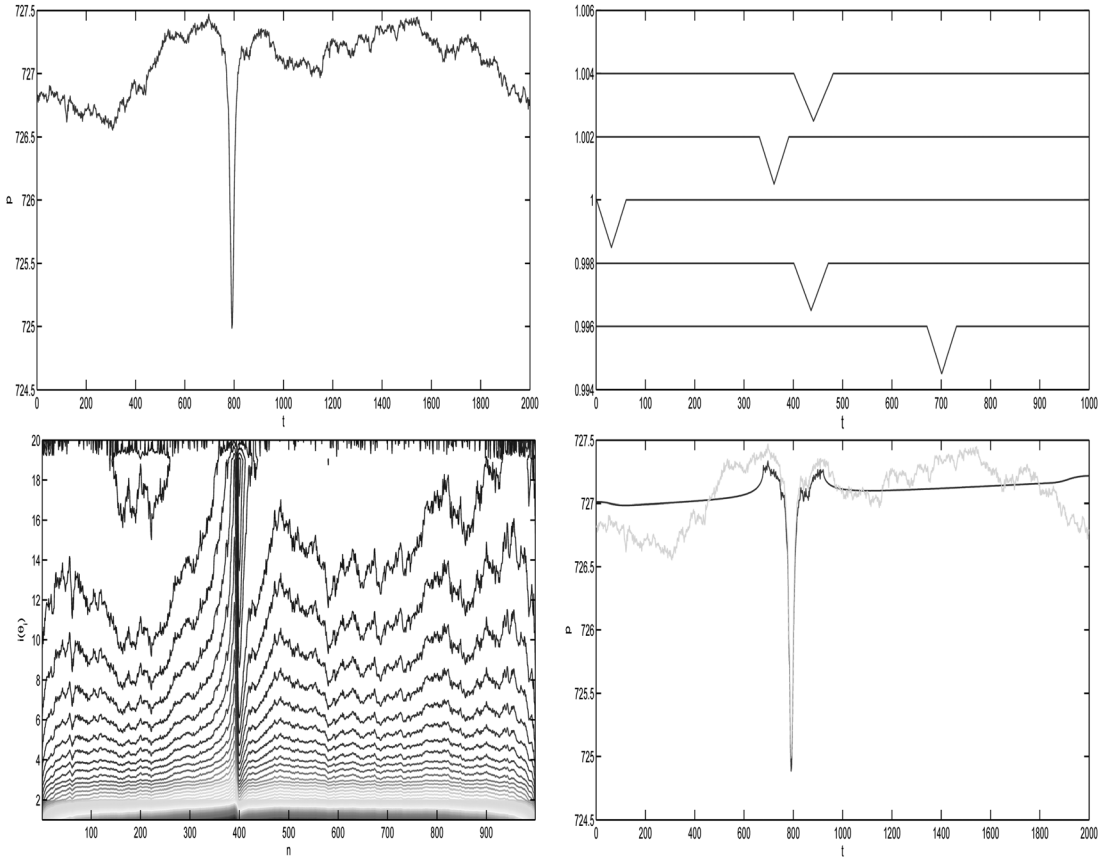

Fig. 6 *Signal, typical signals, the tomogram (coefs 1–999) and the projection on the subspace spanned by the eigenvectors 340–450 and 1000 at $\theta = 19\pi/40$*

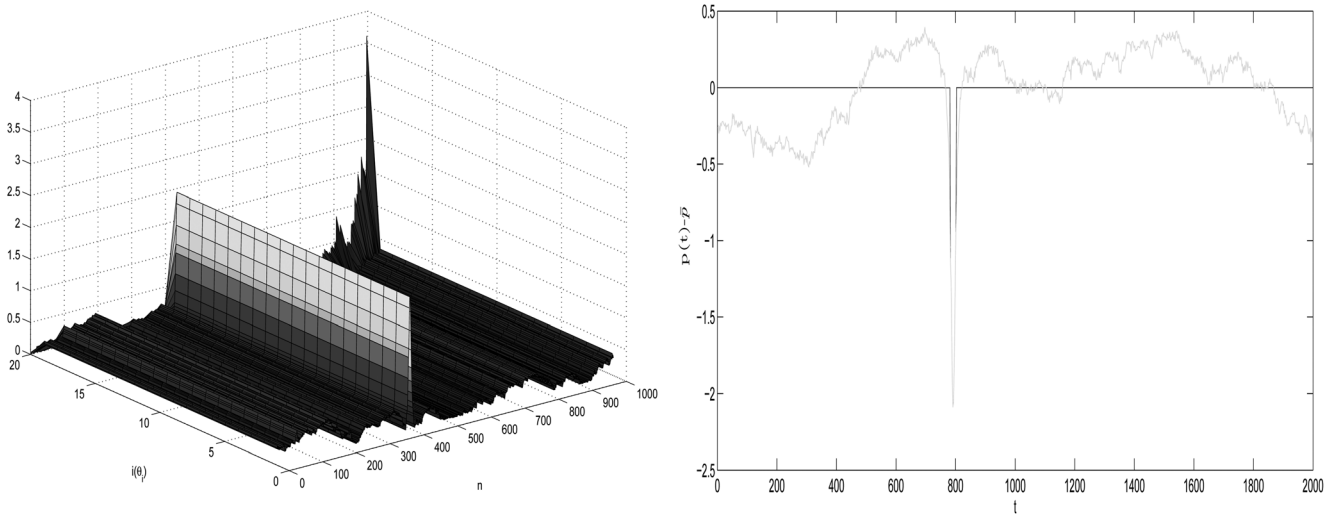

Fig. 7 *Tomogram for 0 mean typical signals and the projection on the subspace spanned by the eigenvectors 340–450 at $\theta = 19\pi/40$*

observe that, aside from the coefficient at $n = 1000$, the strongest components concentrate close to $n = 400$. The lower right panel in Fig. 6 shows the projection on the subspace spanned by the eigenvectors 340–450 and 1000 at $\theta = 19\pi/40$. One sees that the pressure drop produced by the dust devil is very well reconstructed and separated from any other components present in the signal such as noise or smaller pressure variations.

As an alternative, that avoids the large value of the biggest eigenvalue, we may shift both the typical signals and the real data to zero mean signals. In this case there is no eigenvalue much larger than all others. The left panel of Fig. 7 displays a three-dimensional plot of the tomogram for the 1000 coefficients obtained with zero mean signals. We have also applied a denoising procedure, removing the small coefficients. The right panel in Fig. 7 shows the projection on the subspace spanned by the eigenvectors 340–450 at $\theta = 19\pi/40$. One sees that the pressure drop produced by the dust devil is completely separated from any other components in the signal.

4 Conclusions

Tomograms provide a two-variable characterisation of signals which, because of its rigorous probabilistic interpretation, is robust and free of artefacts and ambiguities. For each particular signal that one wants to analyse, the choice of the appropriate tomogram depends not only on the signal but also on the features that we want to identity or emphasise.

We have developed a new family of data-driven tomograms that combines time and an operator obtained from a set of typical signals specially tuned to represent the features that one wants to extract. These adapted tomograms provide, for noisy signals, filtering and separation of components that might not be well represented by standard operators. In fact when passed through Fourier or wavelet analysis both the GPS-like and the dust devil signals used in Section 5 do not provide any useful information, because their relevant features are neither frequency nor scale structure.

5 Acknowledgments

This work was partially supported by the Spanish MICINN BFU2009-08473 and MEIGA METNET PRECURSOR (AYA2011-29967-C05-02) funded by the Spanish 'Ministerio de Economia y Competitividad'. We would also like to thank Germán Martnez for providing the Phoenix Mars Lander data.

6 References

1 Poularikas, A.D. (ed.): 'The transforms and applications handbook' (CRC Press & IEEE Press, Boca Raton, Florida, 1996)
2 Wolf, K.-B.: 'Integral transforms in science and engineering' (Plenum Press, New York, 1979)
3 Fourier, J.B.J.: 'Théorie analytique de la Chaleur', in Darbous, G. (Ed.): Oeuvres de Fourier, (Gauthiers-Villars, Paris, 1888), Tome premier
4 Combes, J.M., Grossmann, A., Tchamitchian, Ph. (eds.): 'Wavelets' (Springer, Berlin, 1990, 2nd edn.)
5 Daubechies, I.: 'The wavelet transform: time–frequency localization and signal analysis', *IEEE Trans. Inf. Theory*, 1990, **36**, (5), pp. 961–1005
6 Chui, C.K. (ed.): 'Wavelets: a tutorial theory and applications' (Academic, Boston, 1992), vol. 2
7 Wigner, E.: 'On the quantum correction for thermodynamic equilibrium', *Phys. Rev.*, 1932, **40**, pp. 749–759
8 Ville, J.: 'Théorie et applications de la notion de signal analytique', *Cables Transm.*, 1948, **2 A**, pp. 61–74
9 Cohen, L.: 'Generalized phase-space distribution functions', *J. Math. Phys.*, 1966, **7**, pp. 781–806
10 Cohen, L.: 'Time–frequency distributions. a review', *Proc. IEEE*, 1989, **77**, pp. 941–981
11 Qian, S., Chen, D.: 'Joint time–frequency analysis' (Prentice-Hall, Englewood Cliffs, NJ, 1995)
12 Husimi, K.: 'Some formal properties of the density matrix', *Proc. Phys. Mat. Soc. Jpn*, 1940, **22**, pp. 264–314
13 Kano, Y.: 'A new phase-space distribution function in the statistical theory of the electromagnetic field', *J. Math. Phys.*, 1965, **6**, pp. 1913–1915
14 Man'ko, V.I., Vilela Mendes, R.: 'Noncommutative time–frequency tomography', *Phys. Lett. A*, 1999, **263**, pp. 53–59
15 Man'ko, M.A., Man'ko, V.I., Vilela Mendes, R.: 'Tomograms and other transforms: a unified view', *J. Phys. A, Math. Gen.*, 2001, **34**, pp. 8321–8332
16 Briolle, F., Man'ko, V.I., Ricaud, B., Vilela Mendes, R.: 'Non-commutative tomography: a tool for data analysis and signal processing', *J. Russ. Laser Res.*, 2012, **33**, pp. 103–121
17 Deans, S.R.: 'The radon transform and some of its applications' (John Wiley & Sons, New York, 1983)
18 Woods, J.C., Barry, D.T.: 'Linear signal synthesis using the Radon–Wigner transform', *IEEE Trans. Signal Process.*, 1994, **42**, pp. 2105–2111
19 Granieri, S., Furlan, W.D., Saavedra, G., Andrés, P.: 'Radon–Wigner display: a compact optical implementation with a single varifocal lens', *Appl. Opt.*, 1997, **36**, pp. 8363–8369
20 Bertrand, J., Bertrand, P.: 'A class of affine Wigner functions with extended covariance properties', *J. Math. Phys.*, 1992, **33**, pp. 2515–2527

doi: 10.1049/iet-spr.2012.0227

21 Goncalvés, P., Baraniuk, R.G.: 'A pseudo-Bertrand distribution for time–scale analysis', *IEEE Signal Process. Lett.*, 1996, **3**, pp. 82–84

22 Huang, N.E., Shen, Z., Long, S.R., *et al*: 'The empirical mode decomposition and the Hilbert spectrum for nonlinear and non-stationary time series analysis', *Proc. R. Soc. London A*, 1998, **454**, pp. 903–995

23 Briolle, F., Lima, R., Man'ko, V.I., Vilela Mendes, R.: 'A tomographic analysis of reflectometry data I: component factorization', *Meas. Sci. Technol.*, 2009, **20**, article id 105501

24 Briolle, F., Lima, R., Vilela Mendes, R.: 'A tomographic analysis of reflectometry data II: the phase derivative', *Meas. Sci. Technol.*, 2009, **20**, pp. 105502

25 Ricaud, B., Briolle, F., Clairet, F.: 'Analysis and separation of time-frequency components in signals with chaotic behavior', arXiv:1003.0734

26 Aguirre, C., Pascual, P., Campos, D., Serrano, E.: 'Single neuron transient activity detection by means of tomography', *BMC Neurosci.*, 2011, **12**, (Suppl 1), p. 297

27 Dente, J.A., Vilela Mendes, R., Lambert, A., Lima, R.: 'The bi-orthogonal decomposition in image processing: signal analysis and texture segmentation', *Signal Process. Image Commun.*, 1996, **8**, pp. 131–148

28 Smith, P.H., Tamppari, L., Arvidson, R.E., *et al*.: 'Introduction to special section on the phoenix mission: landing site characterization experiments, mission over- views, and expected science', *J. Geophys. Res.*, 2008, **113**, article id E00A18

29 de Lucas, E., Miguel, M.J., Mozos, D., Vázquez, L.: 'Martian dust devils detector over FPGA', *Geosci. Instrum. Method. Data Syst.*, 2012, **1**, pp. 23–31